Evolution of triangles in a two-dimensional turbulent flow

Patrizia Castiglione[1,2] and Alain Pumir[3]
[1]*Laboratoire de Physique Statistique, Ecole Normale Supérieure, 24 Rue Lhomond, 75231 Paris Cedex 05, France*
[2]*INFM, Universitàà ''La Sapienza,'' Piazzale A. Moro 2, 00185 Roma, Italy*
[3]*INLN, 1361 Route des Lucioles, F-06560, Valbonne, France*
(Received 23 April 2001; published 24 October 2001)

As a turbulent flow advects a swarm of Lagrangian markers, the mutual separation between particles grows, and the shape of the swarm gets distorted. By following three points in an experimental turbulent two-dimensional flow with a $k^{-5/3}$ spectrum, we investigate the geometry of triangles, in a statistical sense. Two well-characterized shape distributions are identified. At long times when the average size of the triangles $\langle R\rangle$ is larger than the integral scale, the distribution of shapes is Gaussian. When the size of the triangle $\langle R\rangle$ is in the inertial range and grows as $t^{3/2}$ (Richardson's law), a plausibly self-similar, non-Gaussian probability distribution is observed, where very elongated triangles have a much larger probability than in the Gaussian regime. These results are discussed, and, in the latter case, compared with the predictions of a stochastic model recently introduced [A. Pumir *et al.*, Phys. Rev. Lett. **85**, 5324 (2000)].

DOI: 10.1103/PhysRevE.64.056303 PACS number(s): 47.11.+j, 47.27.−i

I. INTRODUCTION

Passive scalar dispersion in a turbulent flow is a problem of both theoretical and practical relevance in many different fields of science and engineering like chemical engineering and geophysics. Some examples are provided by pollutant density, temperature field, and concentration of chemical or biological species in the atmosphere, in the ocean, or in model systems in the laboratory [1].

One of the remarkable aspects of the process is the organization of the passive scalar in fronts of high gradient [2–6]. Also, a very strong intermittency of the scalar statistics has been reported, even when the advecting velocity field is not intermittent as in the case of two-dimensional (2D) turbulence [7–10]. A recent study has shown how these two properties are related in the 2D case: the presence of fronts effectively dominates the statistics of intense fluctuations, resulting in the saturation of the scalar structure function exponents [10].

The structure of the full multipoint correlation function is also sensitive to the coherent structures present in the flow. This has been demonstrated in the case of the passive scalar, in the presence of a mean gradient [11]. The notion of zero modes indeed provides an adequate framework to study the multipoint correlators of the scalar field in the statistically steady state. Their property are intrinsically related to the Lagrangian evolution operator [1,12]. The relation between the structure function of order n and the Lagrangian evolution of n point clusters has been exploited in [9] and a link between the geometrical properties of the turbulent scalar advection and the breakdown of the scale invariance related to intermittency has been established numerically in [12] by studying the evolution of triangles in 2D forced scalar turbulence.

An interesting question about the Lagrangian evolution consists in understanding the dispersion of a swarm of particles of initially fixed shape. We emphasize that the statistical properties of the geometry of dispersing Lagrangian clusters are *not* directly related to the zero modes governing the multipoint correlator evolution and responsible for the appearance of anomalous scaling in scalar turbulence in the statistically steady state problem [7,13–16]. Mathematically, while the zero modes Z_n are the solutions of the equation $\mathcal{H}Z_n=0$ where $\mathcal{H}$ is the evolution operator, the self-similar states S_{sf} predicted in [17] satisfy $\mathcal{H}S_{sf}=(d/dt)S_{sf}$. In the dispersion problem, the zero modes appear only as subdominant corrections to the self-similar behavior. However, it is intuitively very natural to expect that the evolution of the swarm should also provide important information on the geometric structures observed in the flow. Actually, the formation of ''fronts'' is associated with transient domains of hyperbolic flow which distort and ''flatten'' blobs of fluid due to volume preservation. The study of n-point cluster distortion is thus expected to provide insight into the geometric structure of turbulent fluctuations.

One may distinguish several intrinsically different regimes, according to the length scales in the flow. In the inertial range of scales (i.e., when the particle separation is smaller than the largest eddy size), according to Richardson's prediction the dispersion of particle pairs in turbulent flows obeys the superdiffusive law $\langle R^2(t)\rangle\sim t^3$. This law has been observed in 2D both experimentally [18] and numerically [19–21]. At larger scales, one expects the distance between particles to grow according to a diffusive law: $\langle R^2\rangle\propto t$.

The dynamics of three- and four-particle configurations advected by a turbulent flow was studied numerically in three-dimensions (3D) in [17]. By using direct numerical simulation of the Navier-Stokes equation at moderate Reynolds number, and a phenomenological model of the Lagrangian kinematics, the authors predict the existence, within the inertial range of scales, of a self-similar state where the average size of the cluster increases, but the statistical distribution of shapes is stationary and nonuniform. For scales larger than the integral size, the shape distribution is observed to be Gaussian.

In this paper we study the geometrical aspects of Lagrangian dispersion and, in particular, the shape distortion of

 ©2001 The American Physical Society

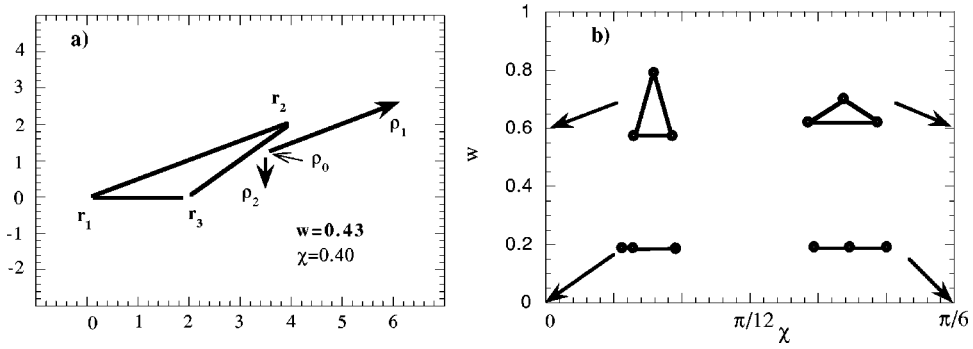

FIG. 1. (a) $\vec{\rho}_1$ and $\vec{\rho}_2$ corresponding to the triangle with $\vec{r}_1=(0,0)$, $\vec{r}_2=(4,2)$, $\vec{r}_3=(2,0)$. The vectors are applied to the center of mass of the triangle $\vec{\rho}_0=(\vec{r}_1+\vec{r}_2+\vec{r}_3)/\sqrt{3}$. (b) Shapes of triangles as a function of w and χ.

small triangles in an experimental 2D turbulent flow in the inverse energy cascade regime. In Sec. II we briefly introduce the parametrization used to describe the size and shape of the triangles. Section III is devoted to the description of our experimental advecting flow and in Sec. IV we report the results of our numerical study. We then (Sec. V) compare our results with those obtained by using the phenomenological model of [17] in the 2D case. We summarize our results and present our conclusions in Sec. VI.

II. TRIANGLE PARAMETRIZATION

In order to describe the size and shape of the triangle corresponding to the points $\vec{r}_1$, $\vec{r}_2$, and $\vec{r}_3$ we have used the Eulerian parametrization as in [22,23]. Introducing

$$\vec{\rho}_1=\frac{(\vec{r}_2-\vec{r}_1)}{\sqrt{2}}, \tag{1}$$

$$\vec{\rho}_2=\frac{(2\vec{r}_3-\vec{r}_2-\vec{r}_1)}{\sqrt{6}}, \tag{2}$$

we define the radius of gyration R characterizing the global size of the triangles by

$$R^2=\vec{\rho_1}^2+\vec{\rho}_2^2=\frac{(r_{12}^2+r_{23}^2+r_{31}^2)}{3}, \tag{3}$$

where $r_{ij}=|\vec{r}_j-\vec{r}_i|$ are the triangle sides, and the variables

$$\chi=\frac{1}{2}\arctan\left[\frac{2\vec{\rho}_1\cdot\vec{\rho}_2}{\rho_2^2-\rho_1^2}\right], \quad w=2\frac{\rho_{11}\rho_{22}-\rho_{12}\rho_{21}}{R^2} \tag{4}$$

for parametrizing the triangle shape. The numerator in the above definition of w is simply the (algebraic) area of the triangle, so $|w|=2\mathcal{A}/(\sqrt{3}R^2)$, where $\mathcal{A}=|\vec{r}_{12}\times\vec{r}_{13}|$.

The two variables w and χ are invariant under dilation, rotation, and translation of the triangle. The parameter space $w\in[-1,1]$, $\chi\in[0,\pi]$ can be reduced to $w\in[0,1]$, $\chi\in[0,\pi/6]$ thanks to the global invariance of the triangles under any relabeling of the three vertices.

In Fig. 1 the $\vec{\rho}_1$ and $\vec{\rho}_2$ vectors corresponding to a scalene triangle are shown (a) and different shapes of triangles are shown as a function of w and χ (b). The isosceles triangles with the third side smaller (larger) than the equal ones correspond to $\chi=0$ ($\chi=\pi/6$). The line $w=0$ corresponds to degenerate configurations, where the three points are aligned. Configurations with both χ and w small correspond to geometries where two vertices (say 1 and 2) are separated by a distance much smaller than the distance to the third: $r_{12}\ll r_{13},r_{23}$. Equilateral triangles correspond to the special case $\vec{\rho}_1\cdot\vec{\rho}_2=0$ and $\rho_1^2-\rho_2^2=0$, that is, to $w=1$ and an undefined value of χ. For triangles of arbitrary shape, the variables w and χ defined in Eq. (4) do not have a simple geometric interpretation.

We investigate here the distribution of parameters characterizing the geometry of the triangles. These include the average value and probability distribution functions (PDF's) of R, w, and χ as functions of time. In this respect we note that the quantity I_2 introduced in [17] as the ratio between the second eigenvalue and the trace of the tensor of moments of inertia, $g_{\alpha\beta}\equiv\Sigma_i\rho_{i\alpha}\rho_{i\beta}$, where $\rho_{i\alpha}$ is the α component of $\vec{\rho}_i$, is very simply related to w by $I_2=(1-\sqrt{1-w^2})/2$.

III. THE TURBULENT VELOCITY FIELD

The experimental velocity field was obtained as described in [24,25]. We recall here the main characteristics of the system used for the preparation of the flow in a steady inverse cascade regime. The flow is generated in a square polyvinyl chloride cell, 15×15 cm^2. The bottom of the cell is made of a thin (1 mm) glass plate, below which permanent magnets, $5\times8\times4$ mm^3 in size, are placed. In order to ensure two-dimensionality, the cell is filled with two layers of NaCl solution, 3 mm thick, with different densities $\delta_1=1030$ g l^{-1} and $\delta_2=1060$ g l^{-1}, placed in a stable configuration, i.e., the heavier underneath the lighter. The interaction of an electrical current driven across the cell with the magnetic field produces local stirring forces. In the experiments we describe here, the experimental conditions of [24] have been exactly reproduced: the magnets are arranged so that the energy is injected, on average, on a scale of $l_i=1.5$ cm; the excitation is permanently maintained. The flow is visualized by tiny latex particles placed at the free surface. During the experiment, the flow is recorded (25 images per second) on a video tape using a charge-coupled device camera placed above the cell. The images are digitized and stored on a computer. We then use standard particle imaging velocimetry techniques to compute the velocity fields every 0.04 s on 64×64 grids. The typical injection Reynolds number of the system (based on the root mean square velocity and the injection scale l_i) is around 100 and

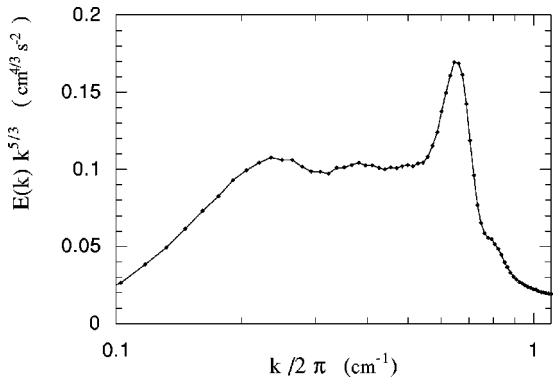

FIG. 2. Compensated energy spectrum $E(k)k^{5/3}$ averaged over the stationary temporal range.

the mean turnover time of the largest eddies is $\tau_v \approx 8$ s.

After a short transient, the flow develops a stationary inverse energy cascade with Kolmogorov-Kraichnan scaling $E(k) \sim k^{-5/3}$. The compensated energy spectrum of the considered velocity field is shown in Fig. 2; the boundaries of the inertial range correspond to the scales $r^I_{min} \simeq 1.5$ cm and $r^I_{max} \simeq 5$ cm. In addition, as reported in [24], the velocity field is homogeneous, isotropic, and nonintermittent.

IV. EVOLUTION OF TRIANGLES IN THE FLOW

The velocity field $\vec{v}(\vec{x},t)$ described in the previous section has been used to calculate numerically the trajectories $\vec{x}(t)$ of particles by integrating the Lagrangian equations

$$\dot{\vec{x}} = \vec{v}(\vec{x},t). \tag{5}$$

The integration of Eq. (5) was performed by using a fourth order Runge-Kutta method with time step $\Delta t = 0.2$ s and a third order interpolation algorithm for the velocity field, defined on a rectangular grid with a lattice spacing $\Delta x = \Delta y = 0.25$ cm [26].

A. Long time asymptotic regime

We studied first the evolution of a set of 2×10^4 initially equilateral triangles with sides of size r_0 equal to 0.25, 1, 4, and 6 cm, respectively. As shown in Fig. 3, the typical size

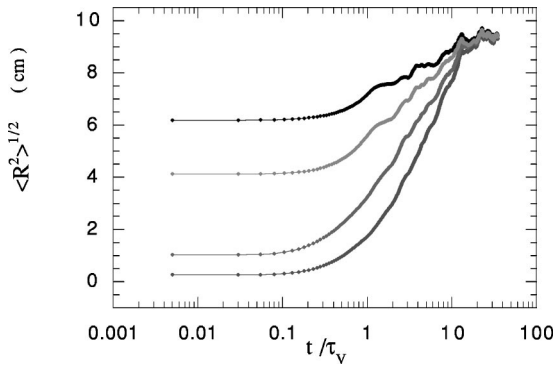

FIG. 3. Temporal evolution of the typical size of the triangles for $r_0 = 0.25$, 1, 4, and 6 cm.

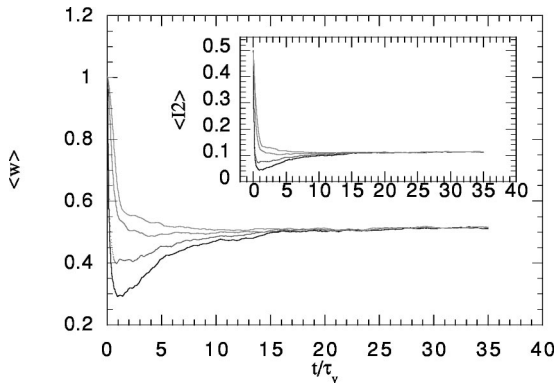

FIG. 4. Temporal evolution of $\langle w \rangle$ for $r_0 = 0.25$, 1, 4, and 6 cm. In the inset, the temporal evolution of $\langle I_2 \rangle$.

$\sqrt{\langle R^2 \rangle}$ of the triangles increases until $t \simeq 13\tau_v$ and fluctuates afterwards around a saturation value of about 9 cm. This is due to the finite size of our experimental cell.

The evolution of $\langle w \rangle$, $\langle I_2 \rangle$ and $\langle \chi \rangle$ as functions of time is shown in Figs. 4 and 5.

As in [17] a rapid decrease of the parameters, corresponding to strong shape distortion of the triangles, is observed; and the smaller the value of r_0, the lower the minimal value of the parameters. When $r_0 = 0.25$ cm the shape distortion is maximum for $\sqrt{\langle R^2 \rangle} \sim 1.5$ cm, the low boundary of the inertial range, while for $\sqrt{\langle R^2 \rangle} \sim 5.5$ cm, around the upper end of the inertial range, the parameters tend to the asymptotic values $\langle w \rangle_{asy} = 0.5$, $\langle \chi \rangle_{asy} = 0.25$, and $\langle I_2 \rangle_{asy} = 0.11$. These values for w and I_2 correspond to a Gaussian distribution of $\vec{\rho}_1$ and $\vec{\rho}_2$, which implies a uniform distribution for w and χ [$\langle w \rangle_{Gau} = 1/2$, $\langle I_2 \rangle_{Gau} = (1 - \pi/4)/2 \approx 0.107$, and $\langle \chi \rangle_{Gau} = \pi/12 \approx 0.262$] and the following distribution for R: $P_{Gau}(R) = (8R^3/\langle R^2 \rangle^2)\exp(-2R^2/\langle R^2 \rangle)$, (see the Appendix). We note a small but significant difference between $\langle \chi \rangle_{asy}$ and $\langle \chi \rangle_{Gau}$.

In Fig. 6, the probability density function evolution of $R/\sqrt{\langle R^2 \rangle}$, w, and χ is shown in the case of $r_0 = 0.25$ cm. We can see that the PDF of R and w can be well approximated by the Gaussian distribution between $t = 80$ s and $t = 100$ s corresponding to $\sqrt{\langle R^2 \rangle}$ between 7.5 cm and 8.6 cm. At later times, because of the saturation of the triangle size, the tails of the distribution of R can no longer be correctly fitted by $P_{Gau}(R)$.

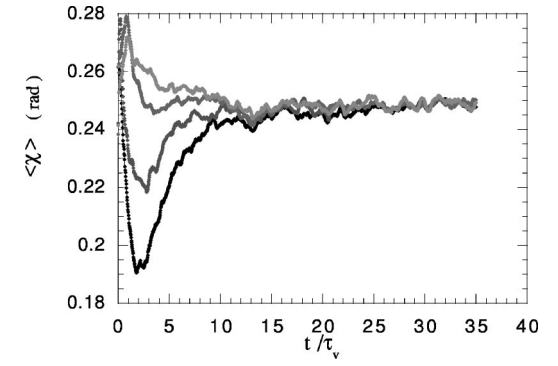

FIG. 5. Temporal evolution of $\langle \chi \rangle$ for $r_0 = 0.25$, 1, 4, and 6 cm.

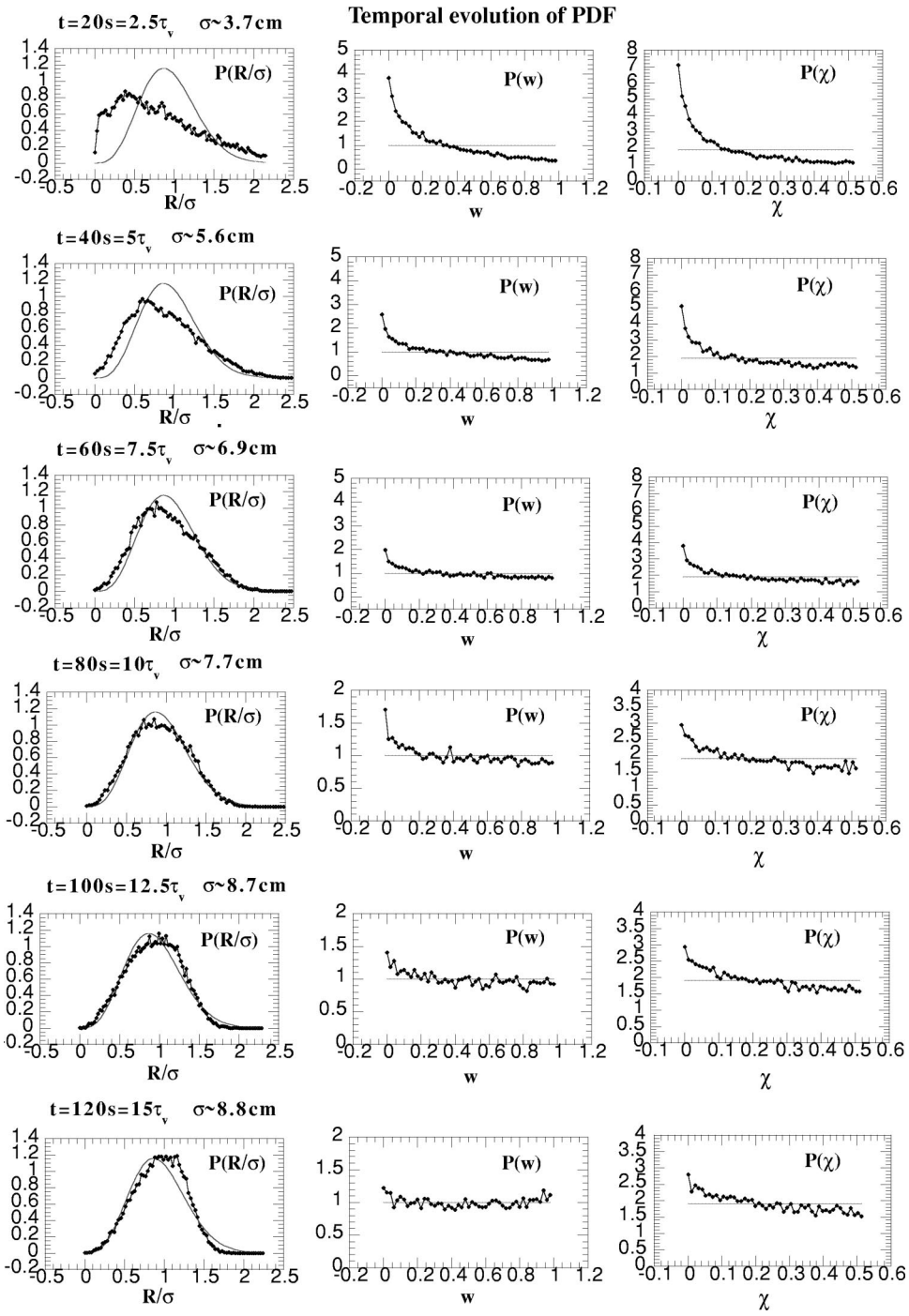

FIG. 6. Temporal evolution of PDF's of R/σ, w, and χ (expressed in radians) for $r_0 = 0.25$ cm. The light lines correspond to the Gaussian predictions $P(R) = 8(R/\sigma)^3 \exp[-2(R/\sigma)^2]$, $P(w)=1$, and $P(\chi)=\pi/6$.

The slight deviation between the observed value $\langle\chi\rangle_{asy}$ and the Gaussian value $\langle\chi\rangle_{Gau}$ has its origin in the PDF of χ, which is *not* constant as a function of χ. We notice that the value $\chi=0$ is (slightly) more probable than the value $\chi=\pi/6$. Geometrically, this means that triangles with a very short edge (two of the three vertices are separated by a distance much smaller than $\sqrt{\langle R^2\rangle}$) have a larger probability than when the three points are taken at random. We believe that this effect is an artifact due to the fact that the diffusive regime cannot be followed for long enough. Indeed, as the triangle size grows larger than the integral size, particle pairs still have a large probability of being very close, which reflects the systematic distortion observed in the inertial range and documented in the following subsection. This effect should disappear if the triangles could be followed for a long enough time.

In Fig. 7 the PDF of $A=wR^2$ proportional to the triangle area is represented for $t=10\tau_v$. Very long tails are observed, which can be well fitted by an exponential function. Note that the PDF of the area is exactly exponential when the distribution of shape is Gaussian (see the Appendix).

The Gaussian distribution of shapes observed at long times corresponds to the regime where the radius of gyration of the triangles grows according to $\sqrt{\langle R^2\rangle}\propto t^{1/2}$, above the

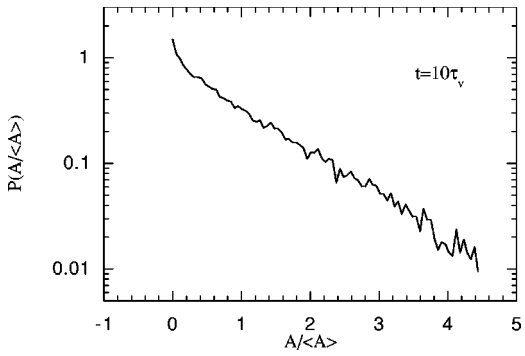

FIG. 7. Probability distribution function of $A = w R^2$, for $r_0 = 0.25$ cm and $t = 10\tau_v$.

integral size of the flow. As shown in Fig. 8, the quantity $\langle R^2 \rangle / t$ exhibits a rather convincing plateau between $t = 3\tau_v$ and $t = 13\tau_v$ when the initial separation is $r_0 = 0.25$ cm (this corresponds in physical units to 3.5 cm$\leqslant \sqrt{\langle R^2 \rangle} \leqslant$9 cm, i.e., in the range between the integral scale $\sim$4 cm and the size of the system $\sim$9 cm. When the initial separation is larger ($r_0 = 1$ cm or $r_0 = 4$ cm), no clear diffusive regime can be seen. This is due to the fact that transients become larger when r_0 is larger, so the asymptotic regime cannot be established before the saturation regime is reached.

In order to check that our results are independent of the presence of the boundaries, we have repeated the numerical analysis in a smaller square of 12×12 cm^2. The results obtained in this case are qualitatively completely similar to those reported here.

In conclusion, we have demonstrated here that the distribution of shapes in the long time, dissipative regime is essentially Gaussian, as expected theoretically, and in agreement with recent numerical simulations [17].

B. The Richardson regime

The flow in our experiment exhibits a $k^{-5/3}$ velocity spectrum over a limited range of scales only (see Fig. 2). Yet it has been possible to observe in a convincing way with this experimental setup the Richardson regime, where particle pairs separate on the average as $\langle R^2 \rangle \propto \epsilon t^3$ [18]. In this subsection, we investigate the problem of triangle dispersion in

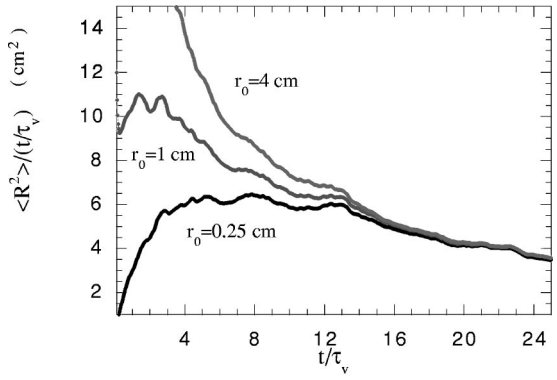

FIG. 8. Compensated temporal behavior of $\langle R^2 \rangle$ for the cases $r_0 = 0.25$, 1, and 4 cm.

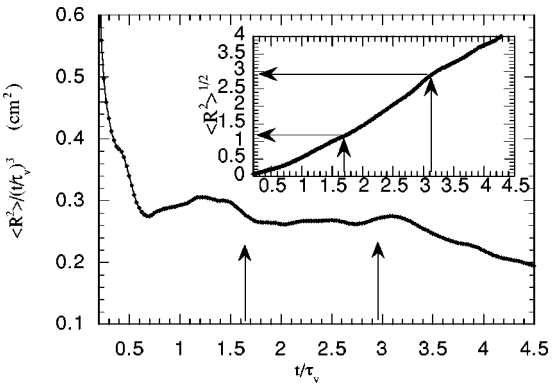

FIG. 9. Compensated temporal behavior of $\langle R^2 \rangle$ in the case of equilateral triangles with $\langle R \rangle = 0.045$ cm. In the inset, the $\sqrt{\langle R^2 \rangle}$ temporal behavior. The plateau between $1.8\tau_v$ and $3.2\tau_v$ corresponds to $\sqrt{\langle R^2 \rangle}$ between 1.25 and 3 cm.

the (limited) inertial range of scale of our experiment. We are interested not only in the growth of the characteristic shape of the triangles, but, more importantly, in the geometrical properties of the triangles as their size grows in the inertial range.

Before we present our experimental results, we emphasize that, in order to obtain the statistical properties of triangles in the inertial range, one needs to make sure that all the separations between the vertices are in the inertial range. In view of the very strong distortion expected theoretically, and indeed observed in the experiment, and of the limited range of inertial scales, this condition is difficult to fulfill. This has to be kept in mind when we discuss our results. However, the experiment shows interesting trends, which we expect will persist in a setup with a larger inertial range of scale.

Our discussion in this section is based on a run with a set of initially 10^5 equilateral triangles with side of size $r_0 = 0.045$ cm ($\langle R \rangle = 0.045$ cm). In this case, a convincing plateau of $\langle R^2 \rangle / t^3$ is reached, as shown in Fig. 9 during about 11 s and correspondingly $\sqrt{\langle R^2 \rangle}$ ranges from 1.25 to 3 cm when $r_0 = 0.045$ cm.

We can explain the fact that the Richardson regime stops at the length 3 cm (see Fig. 9) smaller than the upper limit of

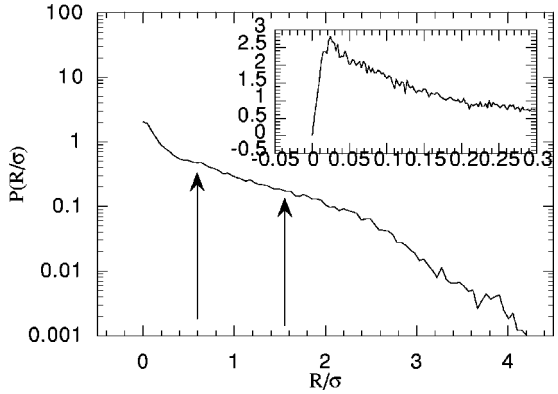

FIG. 10. PDF of R/σ with $\sigma = \sqrt{\langle R^2 \rangle}$ in the case of $r_0 = 0.045$ cm and $t = 2.5\tau_v$. The arrows correspond to the positions of the inertial values of R: $1.25/\sigma$ and $3/\sigma$. In the inset the PDF near $R/\sigma = 0$.

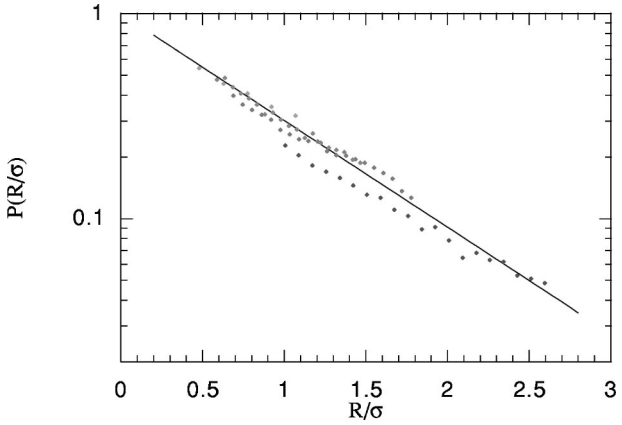

FIG. 11. PDF of R/σ for $(t=1.7,2.2,2.5,3.1)\tau_v$ corresponding to the inertial values of R in the case $r_0=0.045$ cm. The continuous line corresponds to the exponential function $\exp(-1.2x)$.

the inertial range, 5 cm, by recalling that the typical size R is obtained by averaging over the three sides of the triangle. Indeed, for strongly distorted triangles, the longest side of the triangle will reach 5 cm significantly before the radius of gyration $\sqrt{\langle R^2\rangle}$, therefore making the Richardson law invalid well before $\sqrt{\langle R^2\rangle}=5$ cm.

The Richardson $\sqrt{\langle R^2\rangle}\propto t^{3/2}$ regime starts at a scale 1.25 cm slightly smaller than the lower limit of the inertial range (1.5 cm).

In Fig. 10 the PDF of R/σ with $\sigma=\sqrt{\langle R^2\rangle}$ is shown in the $r_0=0.045$ cm and $t=2.5\tau_v$ case. The arrows correspond to the positions of the inertial values of R: 1.25 and 3. The probability distribution functions exhibit a sharp peak near $R=0$, an exponential behavior in the inertial domain, and a decay for *large* values of R slower than an exponential function. The peak occurs for $R/\sigma\sim 0.034$ corresponding to $R=0.04$ cm. We emphasize that the peak is located outside the inertial range, and is very likely to reflect properties associated with the smooth, small scales of the flow.

Figure 11 shows the PDF of R for $t=(1.7,2.2,2.5,3.1)\tau_v$ corresponding to the inertial values of R in the case $r_0=0.045$ cm. The data are slightly dispersed and they could be fitted by the exponential function $\exp(-1.2x)$.

Figure 12 shows the PDF's of w in the case of $r_0=0.045$ cm, for three different times in the Richardson regime. The PDF's are not perfectly stationary and a slight

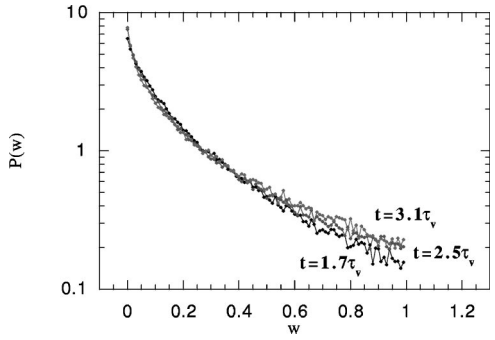

FIG. 12. PDF's of w in the case $r_0=0.045$ cm at different times in the Richardson regime.

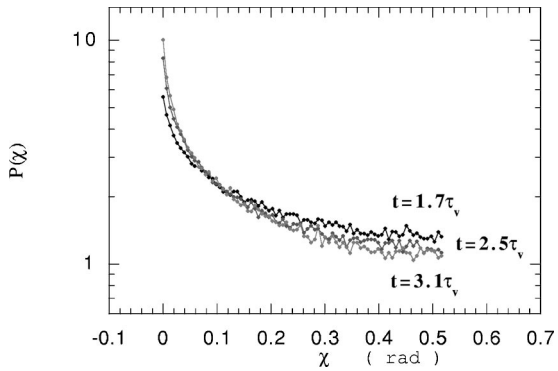

FIG. 13. PDF's of χ in the case $r_0=0.045$ cm at different times in the Richardson regime.

although systematic time dependence of the tails of the distributions is observed. The same behavior occurs for the PDF's of χ as shown in Fig. 13.

The core of the w and χ PDF's is well fitted by the stretched exponential function $\alpha\exp(-\gamma x^{\beta})$ as shown at time $t=2.5\tau_v$ in Fig. 14. The values of the α, β, and γ parameters are indicated in the caption.

We have also calculated the joint probability density function $P(w,\chi)$. In Fig. 15 the contour lines of the logarithm of $P(w,\chi)$ are displayed. The function reaches its maximum for $(w,\chi)=(0,0)$, meaning that the most probable triangles are those with two or three particles stuck together.

The contour lines of the logarithm of the joint PDF $P(w,R/\sigma)$ in the case of $r_0=0.045$ cm are shown in Fig. 16. The maximum of the function is reached for $(w,R/\sigma)\simeq(0,0.034)$, showing that the most probable triangles are stretched and smaller in size than 0.034σ corresponding to $R=0.04$ cm.

The experimental results presented in this section provide strong evidence that the shape distribution of the triangles in 2D, in the inverse energy cascade, is nontrivial, as anticipated in [17].

V. STOCHASTIC MODEL, MONTE CARLO APPROACH

The stochastic model introduced in [17] predicted the existence of a nontrivial shape distribution for triangles advected in a turbulent flow, in the inertial range of scales, on the basis of a study in 3D. The experimental data in the inertial range presented in the previous section invite a comparison with the predictions of this stochastic model in 2D.

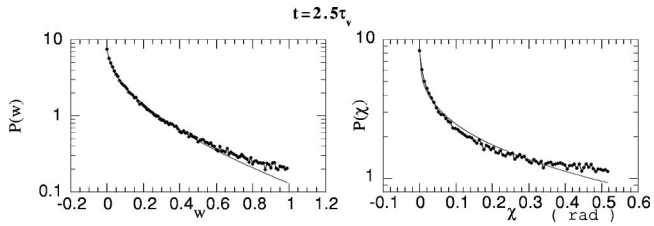

FIG. 14. Best fit of the w and χ PDF's in the case $r_0=0.045$ cm. The chosen function is $\alpha\exp(-\gamma x^{\beta})$ with $\alpha=7.69\pm0.06$, $\beta=0.548\pm0.005$, $\gamma=4.08\pm0.03$ (w), $\alpha=8.6\pm0.2$, $\beta=0.35\pm0.01$, $\gamma=2.8\pm0.05$ (χ).

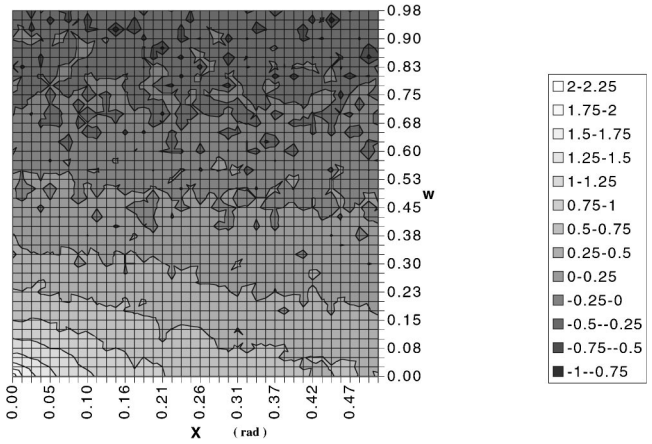

FIG. 15. Contour lines of the logarithm of the joint PDF $P(w,\chi)$ at time $t=2.5\tau_v$ in the case $r_0=0.045$ cm.

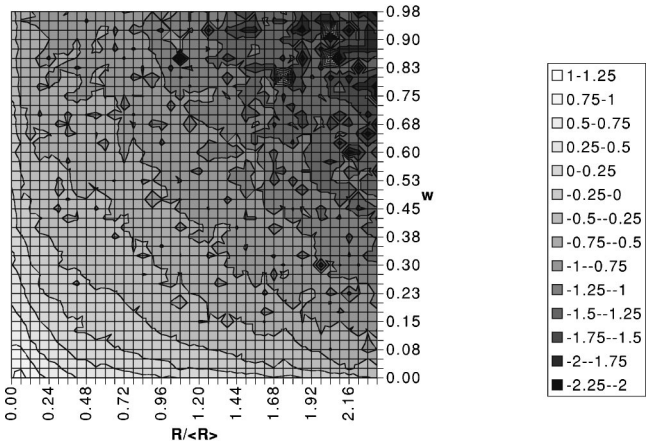

FIG. 16. Contour lines of the logarithm of the joint PDF $P(w,R/\langle R\rangle)$ at time $t=2.5\tau_v$ in the case $r_0=0.045$ cm.

In this section, we recall the physical approximations leading to this model, and compare its predictions with the experimental results.

We emphasize at the outset that the model is of *phenomenological* nature, and has several shortcomings. Its predictions are not expected to be quantitatively accurate. However, as we will explain here, it reproduces correctly several qualitatively important aspects of the solution.

The main idea of the approach consists in using a simplified scale decomposition of the turbulent velocity field. To study the evolution of a triangle with a radius of gyration R, defined as before, we write the velocity field as

$$\vec{v}\equiv\vec{v}_<+\vec{v}_\approx+\vec{v}_> \tag{6}$$

wher $\vec{v}_<$ is the contribution due to the small wave numbers in the usual Fourier decomposition ($|q|\lesssim 1/2R$), $v_>$ comes from the large wave numbers ($|q|\gtrsim 2/R$), and $\vec{v}_\approx$ originates from the scales of the flow comparable to R [$1/(2R)\lesssim|q|\lesssim 2/R$]. The large scale contribution is uniform over the triangle, and simply advects the points without any distortion. As such it is not important for our present purpose. The *like-scale* part of the velocity field, $\vec{v}_\approx$, acts coherently over the scale of the triangles, with a correlation time of the order of $\tau_R=R^{2/3}\epsilon^{-1/3}$. Finally, the small scale component $v_>$ is completely incoherent over the three points, and its correlation time is short compared to τ_R. The action of the turbulent velocity field on the triangle shape is modeled by the following set of stochastic equations:

$$\frac{d\rho_{i\alpha}}{dt}=\rho_{i\beta}M_{\beta\alpha}+u_{i\alpha}, \tag{7}$$

$$\frac{dM_{\alpha\beta}}{dt}=-\frac{M_{\alpha\beta}}{\tau(R)}+\eta_{\alpha\beta}, \tag{8}$$

where latin subscripts label the two vectors $\vec{\rho}_{1,2}$, as before, and greek subscripts represent spatial indices. The u and η terms on the right-hand side (RHS), of Eqs. (7) and (8) are random Gaussian terms, δ correlated in time, with the following variances:

$$\langle\eta_{\alpha\beta}(t)\,\eta_{\mu\nu}(t')\rangle = C_\eta^2\ \delta(t-t')\left(\delta_{\alpha\mu}\delta_{\beta\nu}-\frac{1}{2}\delta_{\alpha\beta}\delta_{\mu\nu}\right)/\tau(R), \tag{9}$$

$$\langle u_{i\alpha}(t)u_{j\beta}(t')\rangle=\left(\frac{C_v}{2}\right)^2\delta(t-t')\,\delta_{ij}\delta_{\alpha\beta}R^2/\tau(R), \tag{10}$$

$$\tau(R)=R^{2/3}\epsilon^{-1/3}. \tag{11}$$

Equation (8) together with Eq. (9) implies that the matrices M are correlated with a time scale $\tau(R)$, and that their amplitudes are of order $|M|\sim R^{-1/3}$. The ρM term in Eq. (7) represents the action of $\vec{v}_\approx$ on the triangle. The random velocity u represents the action of the small scale contribution $\vec{v}_<$. Its time correlation is short; it is represented here by a δ correlated field. The two terms on the RHS of Eq. (7) are of the same magnitude, and they lead to a growth of R according to $\sqrt{\langle R^2\rangle}\propto\epsilon^{1/2}t^{3/2}$. The two dimensionless parameters C_v and C_η give the relative importance of the incoherent jitter and the coherent term, respectively.

Physically, the ρM term in Eq. (7) tends to distort the set of points. Indeed, when $C_v=0$ ($u=0$), the vectors $\vec{\rho}_1$ and $\vec{\rho}_2$ are stretched and aligned under the multiplicative action of a random matrix. At very long times, this process leads to an unbounded distortion.

This effect is opposed by the u term in Eq. (7). In the case where $M=0$ ($C_\eta=0$), the vectors $\vec{\rho}_1$ and $\vec{\rho}_2$ experience the action of an additive, random Gaussian noise. Under these circumstances, the distribution of shapes will be Gaussian: $P(\vec{\rho}_1,\vec{\rho}_2)=[1/\langle R(t)^2\rangle^2\pi^2]\exp[-(\vec{\rho}_1^{\,2}+\vec{\rho}_2^{\,2})/\langle R^2\rangle(t)]$.

The unknown ratio C_v/C_η is *a priori* of order 1 and appears at this stage as a free parameter. Its actual value influences the precise distribution of shapes predicted by the model. For the sake of comparison with the experiments in the present work, we will fix the ratio C_v/C_η by imposing the requirement that the mean values $\langle w\rangle$ and $\langle I_2\rangle$ obtained with the model agree with the observed experimental values.

Note that the Gaussian distribution observed at very long times in the experiment can be explained in this framework.

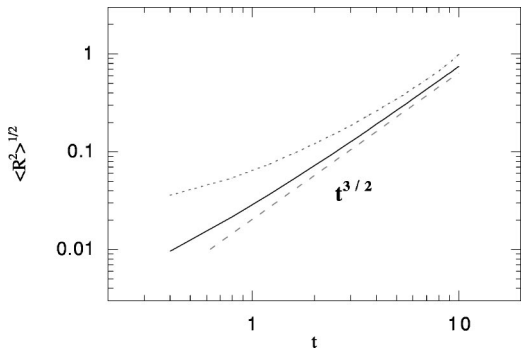

FIG. 17. Temporal evolution of $\langle R^2 \rangle^{1/2}$ for $r_0 = 0.001$ and $r_0 = 0.016$. The spatial units are arbitrary, much smaller than the integral scale and much larger than the dissipative scale. The spatial and temporal units are chosen so that $\epsilon = 1$.

Indeed, at very long times (long compared to the eddy turnover time $\sim L/U$), the separations between particles are larger than the integral scale L, so each particle is advected by a different eddy, acting randomly and independently of all the others. Effectively, one may model the advection by the flow on these time scales by

$$\frac{d\vec{\rho}}{dt} = \vec{u}' \tag{12}$$

with

$$\langle u'^a_i(t) u'^b_j(t') \rangle = C'^2 \delta(t-t') \delta_{ij} \delta_{ab} L^2/\tau(L), \tag{13}$$

effectively leading to the observed Gaussian distribution of shapes.

Before we proceed to study the model in 2D, we wish to point out its limitations. The experimental results presented above, as well as the numerical results in 3D [17], show that the triangles tend to form very elongated structures. In the experiments, it was found that the probability that two of the three vertices of the triangles are very close, compared to the third, is relatively high. For these configurations, it is inappropriate to argue that the relative velocity between the two closest points should behave like $R^{2/3}$, where R is the radius of gyration, as implied by Eqs. (7)–(10). As a consequence, the model tends to diminish the probability of forming triangles with two very close vertices. This should be kept in mind while discussing the results of the model.

The model was integrated numerically by using a straight Monte Carlo algorithm. The time stepping is done by using a classical Euler-Ito scheme of order 1/2 [27]. To prevent occasional underflows, a small scale cutoff, at a scale η much smaller than the characteristic size at $t=0$, is introduced. Statistics over $\sim 10^5$ triangles are accumulated.

Figure 17 shows the evolution of $\sqrt{\langle R^2 \rangle}$ as a function of time, for two values of r_0 ($r_0 = 0.001$ and $r_0 = 0.016$ in our arbitrary units), the initial value of the side of the equilateral triangle. The units are chosen so that $\epsilon = 1$. A convincing regime where $\sqrt{\langle R^2 \rangle}$ grows as $t^{3/2}$ can be clearly seen. The Richardson regime is observed after a transient time, which lasts longer when r_0 is larger. The existence of the $t^{3/2}$ regime is independent of the ratio C_v/C_η.

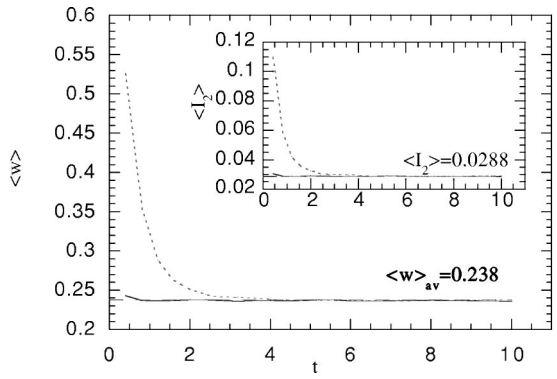

FIG. 18. Temporal evolution of $\langle w \rangle$ for $r_0 = 0.001$ and $r_0 = 0.016$. In the inset, temporal evolution of $\langle I_2 \rangle$.

As a diagnostic of the deformation observed in our model, we monitor the mean values of w and I_2 as a function of time, averaged over all the triangles of the sample. The two quantities relax after a short transient to an equilibrium value, which does not evolve with time (see Fig. 18). This limiting value depends on the ratio C_v/C_η, as seen in Fig. 19. To actually compare with the experiments, we use the values measured experimentally: $\langle w \rangle_{Rich} = 0.23 \pm 0.01$ and $\langle I_2 \rangle_{Rich} = 0.033 \pm 0.003$. For the value of $C_v/C_\eta = 0.45$ indicated by the arrow in Fig. 19 we find $\langle w \rangle_{model} = 0.238$ and $\langle I_2 \rangle_{model} = 0.0288$, very close to the values found experimentally.

The PDF of the radius of gyration for the ratio $C_v/C_\eta = 0.45$ is shown in Fig. 20. The PDF of $R/\langle R \rangle$, corresponding to $t = n\Delta T$, with $\Delta T = 2$ in our arbitrary units, is superposed. This value of ΔT is always much larger than the turnover time at scale $\langle R(t) \rangle$: at the last time in the calculation, $\Delta T/\tau(R) \sim 10$. The distribution at $n=1$, shown by the dashed line, has not quite converged yet, although the $\langle R \rangle \propto t^{3/2}$ growth regime is already reached at this time. In the statistically steady state, the tails of the PDF decay somewhat more slowly than exponentially, as indicated by the slight concavity of the tails in the semilogarithmic plot of Fig. 20, similar to what was observed in Fig. 10. The main, obvious difference comes from the behavior observed at

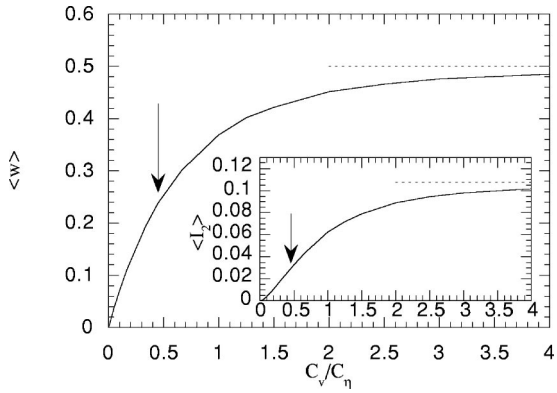

FIG. 19. $\langle w \rangle$ and $\langle I_2 \rangle$ (in the inset) as functions of the ratio C_v/C_η.

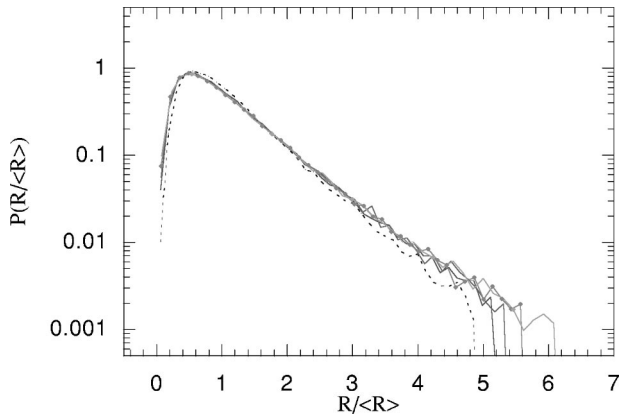

FIG. 20. PDF of $R/\langle R\rangle$ for $t=n\Delta T$ with $\Delta T=2$ and $n=1,\ldots,5$.

small values of $R/\langle R\rangle$. The experimental PDF's are sharply peaked very near 0, whereas the PDF's predicted by the model show a much smoother maximum, around $R/\sqrt{\langle R^2\rangle}\approx 0.45$ (we recall, however, that the value of R where the experimental PDF peaks is significantly below the inertial range).

The PDF of w is shown in Fig. 21. As was the case for the experimental data, the PDF of w decreases monotonically from $w=0$ to $w=1$. The distributions in both cases are therefore biased toward small w, implying, qualitatively, a large probability for very elongated triangles. However, the cuspy aspect of the experimental PDF of w is replaced by a much smoother maximum in the case of the model.

The joint PDF of w and R presented in Fig. 22 shows the same qualitative features as Fig. 16. The isoprobability contours are at a marked angle with the axis $w=0$ and $R/\sqrt{\langle R^2\rangle}=0$, implying that the largest values of R are found preferentially for very small w, i.e., for very distorted triangles. Similarly, very regular triangles (w close to 1) are rare, and are associated with rather small radii of gyration $R/\sqrt{\langle R^2\rangle}$. The differences already reported between the PDF's of $R/\sqrt{\langle R^2\rangle}$ and w can be seen by comparing more precisely the locations of the isoprobability levels of the joint PDF. We find that the isocontours accumulate more toward $(R/\sqrt{\langle R^2\rangle},w)=(0,0)$ in the experimental case than in the

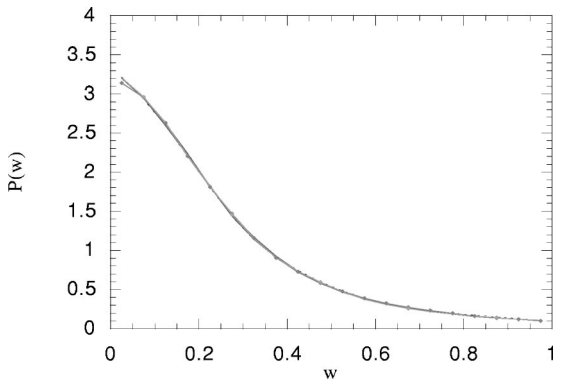

FIG. 21. PDF of $\langle w\rangle$ for $t=n\Delta T$ with $\Delta T=0.4$ and $n=1,\ldots,25$.

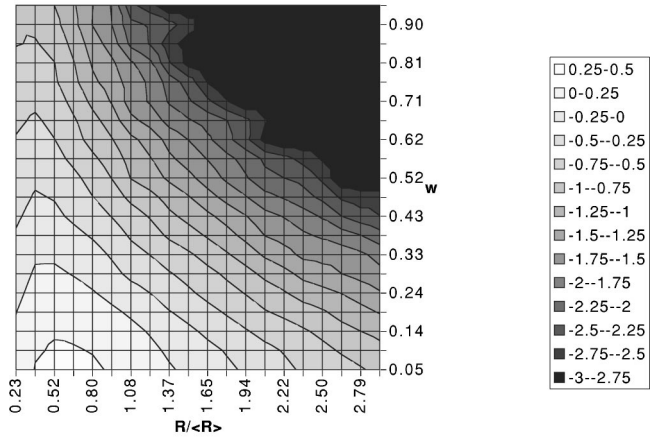

FIG. 22. Contour lines of the logarithm of the joint PDF $P(w,R/\langle R\rangle)$ for the Monte Carlo model.

model prediction. This is in large part due to the large peak of probability near $R/\sqrt{\langle R^2\rangle}=0$ in the experiments.

The PDF of χ, not shown, is found to be completely flat, contary to the experimental PDF, Fig. 13, which shows a cusp near $\chi=0$. The isocontours of the joint PDF of $R/\sqrt{\langle R^2\rangle}$ and χ consist of lines parallel to the $\chi=0$ axis, strongly suggesting that the joint PDF is completely independent of χ.

To summarize our results, we note that the model correctly anticipates the main trends of the distribution of $R/\sqrt{\langle R^2\rangle}$ and w, namely, (i) the tails of the $R/\sqrt{\langle R^2\rangle}$ distributions decay somewhat more slowly than exponentially, (ii) a large fraction of the triangles are very elongated (probability is larger for w close to 0), and (iii) large values of the radius of gyration are associated with very elongated triangles. However, the model systematically underestimates the very sharp peaks observed for both quantities $R/\sqrt{\langle R^2\rangle}$ and w in the experiments. In the same spirit, the model completely misses the sharp dependence of the χ distribution, an effect which can be understood in view of the shortcomings of the model.

VI. DISCUSSION AND CONCLUSIONS

The purpose of this article was to investigate the statistics of the shapes of triangles advected by a 2D turbulent flow. To this end, we have used an experimentally generated flow to follow sets of triangles numerically. The results have been compared with the prediction of a simplified stochastic model, describing the statistics of shapes. Two regimes with well-characterized distributions are identified.

At scales larger than the integral scale, but smaller than the size of the box, a diffusive regime where the mean radius of gyration $\langle R\rangle\propto t^{1/2}$ is observed. The shape distribution of this regime is essentially Gaussian.

When the mean radius of gyration $\langle R\rangle$ is in the (experimentally limited) inertial range of scales, Richardson dispersion is observed ($\langle R\rangle\propto t^{3/2}$), and a plausibly self-similar, nontrivial distribution of shapes is identified. This regime is characterized by an (almost) exponential tail of the PDF of R, and by distributions of w and χ sharply peaked near 0,

contrary to the Gaussian distribution, which is uniform for both variables. These results show that triangles have a higher probability of being elongated than for the purely Gaussian distribution of shapes.

The main limitation of these very suggestive experimental results comes from the limited range of inertial scales. In the Richardson regime, the probability that R is below the inertial range remains relatively important, therefore introducing some biases that should disappear when the inertial range is increased.

Whereas the experimental velocity field exhibits a limited inertial range, we have studied the shape distribution in a 2D turbulent flow with the help of a simplified stochastic model. This model predicts a non-Gaussian, self-similar shape distribution, parametrized by the ratio between the incoherent and coherent components of the flow, acting on the three points. For a realistic value of this ratio, the tails of the PDF of R and the overall shape of the PDF of w qualitatively agree with the exponential PDF's. One strong difference comes from the definition of χ, which is found to be uniform in the model. In general, the probability that two or three particles are very close (separated by a distance smaller than $\langle R\rangle$) is found to be comparatively smaller in the model than experimentally. This phenomenon is partly due to the shortcomings both of the experimental flow (limited inertial range), and of the model, which artificially increases the rate of separation of two close particles when the third particle is far away. This tends to make the distribution of χ even, in particular by diminishing the probability around $(\chi,w)=(0,0)$.

The quantitative differences observed between the experimental distribution and the model predictions can therefore be understood by elementary considerations, related to the deficiencies of the flow and the model. Beyond the discrepancies pointed out, we wish to emphasize that in both cases elongated triangles are observed with a probability significantly higher than in the completely random case. Physically, this can be understood as resulting from the action of the coherent, strainlike component of the velocity field which tends to align all points. The effect of alignment of particles in a particular direction of the strain, coarse grained at the scale characterizing the set of points, should persist both in the case of clusters with more than three points, and in higher dimensions $(D=3)$.

ACKNOWLEDGMENTS

We are particularly grateful to M. C. Jullien and P. Tabeling for their support. We thank M. Vergassola and A. Celani for stimulating discussions and suggestions. We acknowledge the support of the European Commission's TMR program, Contract No. ERBFMRXCT980175, ''Intermittency in turbulent systems.'' The continuous support in computer time from IDRIS in Paris is gratefully acknowledged.

APPENDIX: THE GAUSSIAN SHAPE DISTRIBUTION FOR TRIANGLES IN TWO DIMENSIONS

Let us assume that the two vectors, defined by Eq. (2), are distributed according to the Gaussian distribution

$$P(\vec{\rho}_1,\vec{\rho}_2)=\frac{4}{\pi^2\langle R^2\rangle^2}\exp[-2(\vec{\rho}_1^{\,2}+\vec{\rho}_2^{\,2})/\langle R^2\rangle]. \quad \text{(A1)}$$

We reexpress in this Appendix the PDF P in terms of the variables introduced to characterize the shape of the triangles. The vectors $\vec{\rho}_1$ and $\vec{\rho}_2$ are decomposed according to [22,23]

$$\vec{\rho}_1=\xi_1\cos\chi\hat{e}_1(\phi)+\xi_2\sin\chi\hat{e}_2(\phi),$$

$$\vec{\rho}_2=-\xi_1\sin\chi\hat{e}_1(\phi)+\xi_2\cos\chi\hat{e}_2(\phi) \quad \text{(A2)}$$

with $\hat{e}_1(\phi)=(\cos\phi,\sin\phi)$ and $\hat{e}_2(\phi)=(-\sin\phi,\cos\phi)$. The angle ϕ is a rotation angle, with respect to a fixed orthogonal basis. A straightforward calculation leads to the following result for the Jacobian of the transformation $(\xi_1,\xi_2,\chi,\phi)\rightarrow(\rho_{11},\rho_{12},\rho_{21},\rho_{22})$, where $\rho_{i,j}$ is the jth component of $\vec{\rho}_i$:

$$\left|\frac{D(\rho_{11},\rho_{12},\rho_{21},\rho_{22})}{D(\xi_1,\xi_2,\chi,\phi)}\right|=|\xi_2^2-\xi_1^2|, \quad \text{(A3)}$$

so the PDF expressed in the variables ξ_1, ξ_2, χ, and ϕ is

$$P(\xi_1,\xi_2,\chi,\phi)=P(\rho_{11},\rho_{12},\rho_{21},\rho_{22})\left|\frac{D(\rho_{11},\rho_{12},\rho_{21},\rho_{22})}{D(\xi_1,\xi_2,\chi,\phi)}\right|$$

$$=\frac{4}{\pi^2\langle R^2\rangle^2}\exp[-2(\xi_1^2+\xi_2^2)/\langle R^2\rangle]|\xi_2^2-\xi_1^2|. \quad \text{(A4)}$$

Introducing further $R=\sqrt{\vec{\rho}_1^{\,2}+\vec{\rho}_2^{\,2}}=\sqrt{\xi_1^2+\xi_2^2}$ and $w=2\xi_1\xi_2/(\xi_1^2+\xi_2^2)$, the Jacobian of the transformation $(\xi_1,\xi_2)\rightarrow(R,w)$ is

$$\left|\frac{D(R,w)}{D(\xi_1,\xi_2)}\right|=\frac{2|\xi_2^2-\xi_1^2|}{R^3}. \quad \text{(A5)}$$

Combining Eqs. (A4) and (A5), one finds that the Gaussian PDF of shapes, expressed with R, w, χ, and ϕ is simply

$$P(R,w,\chi,\phi)=\frac{8}{\langle R^2\rangle^2}R^3\exp(-2R^2/\langle R^2\rangle). \quad \text{(A6)}$$

Equation (A6) implies that the probabilities of the variables χ and w are both uniform, which implies that the Gaussian mean values are $\langle\chi\rangle_{gau}=\pi/12$ and $\langle w\rangle_{gau}=1/2$.

With the distribution of R and w, it is straightforward to compute the PDF of the area $A=wR^2$. Indeed,

$$P(A)=\frac{8}{\langle R^2\rangle^2}\int dR\,dw\,\delta(A-wR^2)R^3\exp(-2R^2/\langle R^2\rangle)$$

$$=\frac{8}{\langle R^2\rangle^2}\int_{\sqrt{A}}^{\infty}dR\,R\exp(-2R^2/\langle R^2\rangle)$$

$$=\frac{2}{\langle R^2\rangle}\exp(-2A/\langle R^2\rangle). \quad \text{(A7)}$$

The quantity I_2, used to characterize the shape distortion, is defined as the ratio of the second eigenvalue of the mo-

ment of inertia tensor and R^2. This quantity can be expressed, in the case of triangles in two-dimensions, as $I_2 = (1-\sqrt{1-w^2})/2$. The mean value, in the sense of the Gaussian distribution of I_2, can be simply computed by using the fact that $p(w)=1$. Introducing the change of variable $w=\sin\theta$ $(0 \leqslant \theta \leqslant \pi/2)$, we have $p(\theta)=dw/d\theta=\cos\theta$ and $I_2=(1-\cos\theta)/2$, implying that

$$\int_0^{1/2} dI_2 I_2 P(I_2) = \int_0^{\pi/2} d\theta \frac{1}{2}(1-\cos\theta)\cos\theta = \frac{1}{2}\left(1-\frac{\pi}{2}\right). \tag{A8}$$

The mean value of I_2 is thus $\langle I_2 \rangle_{gau} = (1-\pi/4)/2$.

[1] B.I. Shraiman and E.D. Siggia, Nature (London) **405**, 639 (2000).
[2] K.R. Sreenivasan, Proc. R. Soc. London, Ser. A **434**, 165 (1991).
[3] P.G. Mestayer, J. Fluid Mech. **125**, 475 (1982).
[4] M. Holzer and E. Siggia, Phys. Fluids **6**, 1820 (1994).
[5] A. Pumir, Phys. Fluids **6**, 2118 (1994).
[6] S. Chen and R.H. Kraichnan, Phys. Fluids **10**, 2867 (1998).
[7] B.I. Shraiman and E.D. Siggia, C. R. Acad. Sci., Ser. IIb: Mec., Phys., Chim., Astron. **321**, 279 (1995).
[8] L. Mydlarski and Z. Warhaft, J. Fluid Mech. **320**, 135 (1998).
[9] U. Frisch, A. Mazzino, and M. Vergassola, Phys. Rev. Lett. **80**, 5532 (1998).
[10] A. Celani, A. Lanotte, A. Mazzino, and M. Vergassola, Phys. Rev. Lett. **84**, 2385 (2000).
[11] L. Mydlarski, A. Pumir, B.I. Shraiman, E.D. Siggia, and Z. Warhaft, Phys. Rev. Lett. **81**, 4373 (1998).
[12] A. Celani and M. Vergassola, Phys. Rev. Lett. **86**, 424 (2001).
[13] M. Chertkov, G. Falkovich, I. Kolokolov, and V. Lebedev, Phys. Rev. E **52**, 4924 (1995).
[14] K. Gawedzki and A. Kupiainen, Phys. Rev. Lett. **75**, 3834 (1995).
[15] O. Gat and R. Zeitak, Phys. Rev. E **57**, 5511 (1998).
[16] O. Gat, I. Procaccia, and R. Zeitak, Phys. Rev. Lett. **80**, 5536 (1998).
[17] A. Pumir, B.I. Shraiman, and M. Chertkov, Phys. Rev. Lett. **85**, 5324 (2000).
[18] M.C. Jullien, J. Paret, and P. Tabeling, Phys. Rev. Lett. **82**, 2872 (1999).
[19] A. Babiano, C. Basdevant, P. Le Roy, and R. Sadourny, J. Fluid Mech. **214**, 535 (1990).
[20] G. Boffetta, A. Celani, A. Crisanti, and A. Vulpiani, Europhys. Lett. **46**, 177 (1999).
[21] G. Boffetta, A. Celani, A. Crisanti, and A. Vulpiani, Phys. Rev. E **60**, 6734 (1999).
[22] B.I. Shraiman and E.D. Siggia, Phys. Rev. E **57**, 2965 (1998).
[23] A. Pumir, Phys. Rev. E **57**, 2914 (1998).
[24] J. Paret and P. Tabeling, Phys. Fluids **10**, 3126 (1998).
[25] J. Paret and P. Tabeling, Phys. Rev. Lett. **79**, 4162 (1997).
[26] W.H. Press, S.A. Teukolsky, W.T. Vetterling, and B.F. Flannery, *Numerical Recipes: The Art of Scientific Computing* (Cambridge University Press, Cambridge, 1991).
[27] P.E. Kloeden and E. Platen, *Numerical Solutions of Stochastic Differential Equations* (Springer, Berlin, 1992).